

Spatio-temporal dynamics near a supercritical Turing-Hopf bifurcation in a two-dimensional reaction-diffusion system

W. Just^{1,2)*†}, M. Bose¹⁾, S. Bose¹⁾, H. Engel¹⁾, and E. Schöll¹⁾

¹⁾ Institut für Theoretische Physik, Technische Universität Berlin,
Hardenbergstr. 36, D-10623 Berlin, Germany

²⁾ School of Mathematical Sciences, Queen Mary & Westfield College,
Mile End Road, London E1 4NS, UK

May 3, 2001

Abstract

Pattern formation in semiconductor heterostructures is studied on the basis of a spatially two-dimensional model of reaction-diffusion type. In particular, we investigate the neighbourhood of a codimension-two Turing-Hopf instability by analytical methods. Amplitude equations are derived which predict the absence of mixed modes but extended ranges of bistability between homogeneous oscillatory states and hexagonal Turing patterns. Our results are confirmed by numerical simulations. The features are not confined to a neighbourhood of the bifurcation point so that the conclusions of the weakly nonlinear analysis explain the observations in large portions of the parameter space at least qualitatively

1 Introduction

Pattern formation in systems far from equilibrium is one of the most challenging fields in modern nonequilibrium physics. There exists a variety of investigations in quite different physical contexts like optical, magnetic, or chemical systems [1, 2] but a unifying perspective is still missing. Some universal aspects which are independent from the underlying microscopic and mesoscopic details appear usually near stability thresholds and can be treated theoretically by some kind of normal form approach. Thus one gets an effective motion for slow degrees of freedom which allows to understand the spatio-temporal dynamics to some extent.

Particularly interesting features appear if instabilities are considered where different modes compete. One prominent example is given by Turing-Hopf instabilities [3]. Here two modes exhibiting a purely spatially or temporarily periodic pattern, respectively, occur simultaneously giving rise to mixed spatio-temporal periodic patterns, domain structures displaying bistability between spatial and temporal modes, and space-time chaos. Such features have been confirmed even experimentally e.g. in the hydrodynamic context [4, 5] or in chemical reaction-diffusion systems [6, 7].

Here we are concerned with models which have been developed in the context of semiconductor charge transport in heterostructure devices [8]. These models are able to describe nonequilibrium patterns formation in layered structures like the heterostructure hot electron diode [9], p-n-p-n diodes [10, 11] and p-i-n diodes [12] or in impurity impact ionisation breakdown [13, 14]. The models

*e-mail: W.Just@qmw.ac.uk

†present address: Institut für Physik, TU-Chemnitz, D-91071 Chemnitz, Germany

we are concerned with fall in the larger class of reaction–diffusion models of activator–inhibitor type which have been extensively studied throughout the last decade.

In particular, we focus on the following spatially two–dimensional model of reaction–diffusion type which describes pattern formation in layered semiconductor devices

$$\begin{aligned}\frac{\partial u}{\partial t} &= \alpha[j_0 - (u - a)] + D\Delta u \\ \frac{\partial a}{\partial t} &= f(u - a) - Ta + \Delta a \quad .\end{aligned}\tag{1}$$

Here Δ denotes the two–dimensional Laplacian and the nonlinear part of the transport equation reads

$$f(v) := \frac{v}{1 + v^2} \quad .\tag{2}$$

In physical terms the dynamical observables are given by the dimensionless voltage across the heterostructure $u(\mathbf{r}, t)$ and an internal degree of freedom, $a(\mathbf{r}, t)$, e.g., the dimensionless interface charge density. Here a and u play the roles of activator and inhibitor, respectively. D denotes an effective diffusion constant and T the tunnelling rate. The two important system parameters are given by the total current j_0 and the relaxation rate α . For additional physical background of the model we refer the interested reader to the literature [15]. Patterns in one spatial dimension near a codimension–two Turing–Hopf bifurcation were analysed in [16, 17, 18]. Variants of eqs.(1) with a global constraint were studied in [19, 20]. In contrast to previous investigations here we focus on the physically relevant spatially two–dimensional case which is known in general to be much more challenging compared to one–dimensional pattern formation, cf., for instance, results obtained for the globally coupled model [21, 22] or investigations in reaction diffusion like systems [23]. We review the linear stability analysis of our model in section 2 in order to keep the presentation self contained. We are in particular interested in the behaviour near the codimension–two Turing–Hopf point. Section 3 is devoted to an analytical approach in terms of amplitude equations. Thus, we are able to predict which type of pattern appears beyond the stability threshold. Those readers who are primarily interested in properties of the solutions of our system (1) may skip the analytical part at the first inspection and may consult directly section 4 where the analytical results are compared with numerical solutions. Some technical details are contained in two appendices.

2 Linear stability analysis

For our theoretical analysis we impose periodic boundary conditions and consider eventually the limit of infinite system size so that boundary effects are assumed to be negligible. In order to study the pattern formation in system (1) let us begin with the spatially homogeneous fixed point

$$u_* = j_0 + \frac{1}{T}f(j_0), \quad a_* = \frac{1}{T}f(j_0) \quad ,\tag{3}$$

and dwell on its stability. Since a detailed analysis can be found in the literature [17] we just quote the necessary results and set up the notation for the weakly nonlinear analysis. Considering small deviations from the fixed point (3)

$$\Phi_1 = u - u_*, \quad \Phi_2 = u - u_* - (a - a_*)\tag{4}$$

the equation of motion (1) up to third order reads

$$\frac{\partial \Phi_1}{\partial t} = D\Delta \Phi_1 - \alpha \Phi_2$$

$$\begin{aligned} \frac{\partial \Phi_2}{\partial t} = & T\Phi_1 + (D-1)\Delta\Phi_1 - [\alpha + T + f'(j_0)]\Phi_2 + \Delta\Phi_2 \\ & - \frac{1}{2}f''(j_0)\Phi_2\Phi_2 - \frac{1}{6}f'''(j_0)\Phi_2\Phi_2\Phi_2 + \mathcal{O}(\Phi^4) \quad . \end{aligned} \quad (5)$$

Linear stability is easily analysed in terms of Fourier modes and is governed by the eigenvalues of the 2×2 matrix

$$\underline{L}(k) = \begin{pmatrix} -Dk^2 & -\alpha \\ T - (D-1)k^2 & -(\alpha + T + f'(j_0)) - k^2 \end{pmatrix} \quad , \quad (6)$$

where k denotes the modulus of the wavenumber of the Fourier mode.

The condition for a Turing instability requires that the matrix (6) admits a single zero eigenvalue at a critical wavenumber with modulus $q_c \neq 0$. Real parts of all other eigenvalues have to be negative. These conditions result in

$$\left(\sqrt{T} + \sqrt{\frac{\alpha^T}{D}} \right)^2 + f'(j_0^T) = 0 \quad (7)$$

with the critical wavenumber being given by

$$q_c = \left(\frac{\alpha^T T}{D} \right)^{1/4} \quad . \quad (8)$$

Right- and left-eigenvectors of the matrix $\underline{L}(q_c)$ corresponding to the critical eigenvalue read

$$\underline{u}_c = \begin{pmatrix} -\alpha^T \\ Dq_c^2 \end{pmatrix}, \quad \underline{v}_c^* = (T - [D-1]q_c^2, Dq_c^2) \quad . \quad (9)$$

A Hopf bifurcation appears if the matrix (6) possesses a pair of purely imaginary complex conjugated eigenvalues at $k = 0$. The condition on the parameters reads

$$\alpha^H + T + f'(j_0^H) = 0 \quad , \quad (10)$$

where

$$\omega_c = \sqrt{\alpha^H T} \quad (11)$$

denotes the imaginary part of the eigenvalue. The corresponding right- and left-eigenvectors are easily evaluated as

$$\underline{\tilde{u}}_c = \begin{pmatrix} -\alpha^H \\ i\omega_c \end{pmatrix}, \quad \underline{\tilde{v}}_c^* = (-T, -i\omega_c) \quad . \quad (12)$$

We shall consider fixed values for the diffusion coefficient D and the tunnelling rate T . Then eqs.(7) and (10) describe bifurcation lines in the parameter plane being spanned by the current j_0 and the relaxation rate α (cf. figure 1). Crossing these bifurcation lines the pattern formation can be studied by weakly nonlinear analysis in terms of amplitude equations. In that context the intersection points of the bifurcation lines, i.e. the Turing-Hopf bifurcations, are of particular importance. Here the interaction of the different weakly unstable modes causes interesting features which can be studied within an analytical framework. Parameter values of these degenerate bifurcations are obtained from eqs.(7) and (10)

$$\alpha^{\text{TH}} + T + f'(j_0^{\text{TH}}) = 0, \quad 4DT = \alpha^{\text{TH}}(D-1)^2 \quad , \quad (13)$$

where

$$q_c^{\text{TH}} = \sqrt{\frac{2T}{D-1}}, \quad \omega_c^{\text{TH}} = \sqrt{\alpha^{\text{TH}} T} \quad (14)$$

denote the critical wavenumber and the frequency at the codimension-two point, respectively. The behaviour of the system in the vicinity of this degenerate bifurcation point is at the centre of interest in the following section.

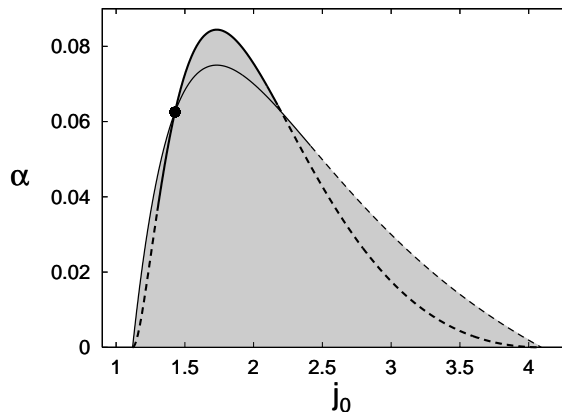


Figure 1: Bifurcation lines for the Turing (thick line) and the Hopf instability (thin line) in the j_0 - α parameter plane for $D = 5$ and $T = 0.05$. Broken/solid lines indicate that the bifurcation is sub/supercritical (cf. section 3). Grayshading marks the region where the trivial fixed point is unstable. The lefthand Turing–Hopf point is indicated.

3 Weakly nonlinear analysis near the codimension–two point

The behaviour in the vicinity of the bifurcation lines can be investigated by means of a weakly nonlinear analysis. The spirit of such a standard approach is quite simple and we only quote the essential steps here. The solution of eq.(5) is expanded as

$$\underline{\Phi} = \kappa \sum_{\ell} (A_{\ell} \exp[i\mathbf{q}_{\ell}\mathbf{r}]\underline{u}_c + c.c.) + \kappa (B \exp[i\omega_c t]\underline{\tilde{u}}_c + c.c.) + \kappa^2 \underline{\Phi}^{(2)} + \kappa^3 \underline{\Phi}^{(3)} + \dots, \quad (15)$$

where the square of the expansion parameter κ denotes the distance from the bifurcation line in parameter space, and the superscripts (2), (3) mark second and third order terms, respectively. The moduli of all wave vectors \mathbf{q}_{ℓ} coincide with the critical value q_c .

The type of mode which appears in the ansatz (15) depends on whether we are considering the Turing, the Hopf, or the Turing–Hopf instability. For the analysis of Turing instabilities in more than one spatial dimension no general approach exists. One has to fix the particular critical wavevectors beforehand. Here we are focusing on three prominent types of patterns: (a) plane waves consisting of a single wave vector, (b) square patterns being determined by two orthogonal wave vectors, and (c) hexagonal patterns where three wave vectors in C_3 symmetric configuration appear.

Substituting the ansatz (15) into eq.(5) and expanding up to third order one obtains amplitude equations for the slowly varying amplitudes A and B . To facilitate the notation we introduce the abbreviations

$$C\{\underline{\phi}, \underline{\psi}\} = -\frac{1}{2}f''(j_0) \begin{pmatrix} 0 \\ \phi_2 \psi_2 \end{pmatrix}, \quad D\{\underline{\phi}, \underline{\psi}, \underline{\chi}\} = -\frac{1}{6}f'''(j_0) \begin{pmatrix} 0 \\ \phi_2 \psi_2 \chi_2 \end{pmatrix} \quad (16)$$

so that the quadratic and cubic contributions of eq.(5) are given by $C\{\underline{\Phi}, \underline{\Phi}\}$ and $D\{\underline{\Phi}, \underline{\Phi}, \underline{\Phi}\}$. For some technical details of the derivation we refer the reader to appendix A.

In our analysis we discard sideband instabilities, i.e. we only take a time dependence on slow time scales τ into account. A full analysis containing also spatial dependencies on slowly varying

scales is much more cumbersome and seems to be not necessary for our purpose since no sideband instabilities show up in our simulations.

3.1 The codimension–one cases

Let us first recall the features occurring near the bifurcation lines. For the Hopf instability only mode B appears in the ansatz (15). If $\kappa^2 \delta \alpha = \alpha - \alpha^{\text{H}}$ and $\kappa^2 \delta j_0 = j_0 - j_0^{\text{H}}$ denote the distance from the Hopf bifurcation line (10) the just mentioned analysis results in the amplitude equation

$$\frac{\partial B}{\partial \tau} = \eta B + \hat{\gamma} |B|^2 B \quad . \quad (17)$$

Let $\langle \cdot, \cdot \rangle$ denote the canonical inner product and $\delta \underline{L}(0)$ the change of the matrix (6) due to the deviation of the parameters from the Hopf bifurcation line. Then the linear coefficient of eq.(17) reads

$$\begin{aligned} \eta &= \frac{\langle \tilde{\underline{v}}_c | \delta \underline{L}(0) \tilde{\underline{u}}_c \rangle}{\langle \tilde{\underline{v}}_c | \tilde{\underline{u}}_c \rangle} \\ &= \frac{i \omega_c T \delta \alpha - \omega_c^2 (\delta \alpha + f''(j_0^{\text{H}}) \delta j_0)}{2 \omega_c^2} \quad . \end{aligned} \quad (18)$$

For the cubic coefficient we use the general expression (cf. e.g. [24])

$$\begin{aligned} \hat{\gamma} &= \frac{1}{\langle \tilde{\underline{v}}_c | \tilde{\underline{u}}_c \rangle} \langle \tilde{\underline{v}}_c | 4C\{\tilde{\underline{u}}_c, \tilde{\underline{\Gamma}}_a\} + 2C\{\tilde{\underline{u}}_c^*, \tilde{\underline{\Gamma}}_b\} + 3D\{\tilde{\underline{u}}_c, \tilde{\underline{u}}_c, \tilde{\underline{u}}_c^*\} \rangle \\ \tilde{\underline{\Gamma}}_a &:= -\frac{1}{\underline{L}(0)} C\{\tilde{\underline{u}}_c, \tilde{\underline{u}}_c^*\} \\ \tilde{\underline{\Gamma}}_b &= -\frac{1}{\underline{L}(0) - 2i\omega_c \underline{1}} C\{\tilde{\underline{u}}_c, \tilde{\underline{u}}_c\} \quad . \end{aligned} \quad (19)$$

Evaluation with the help of eqs.(6), (12), and (16) yields

$$\hat{\gamma} = \frac{\omega_c^2}{2} \left[-\frac{i}{3\omega_c} (f''(j_0^{\text{H}}))^2 - \frac{1}{2} f'''(j_0^{\text{H}}) \right] \quad . \quad (20)$$

The crucial point is the sign of $\text{Re} \hat{\gamma}$. It determines whether the bifurcation is sub- or supercritical (cf. figure 1). The positive and negative signs correspond to sub- and supercritical, respectively.

Let us now treat the vicinity of the Turing bifurcation line (7) in the same way, thus $\kappa^2 \delta \alpha = \alpha - \alpha^{\text{T}}$ and $\kappa^2 \delta j_0 = j_0 - j_0^{\text{T}}$. If we first confine ourselves to plane waves, i.e. a single amplitude A appears in the ansatz (15), then the resulting amplitude equation reads

$$\frac{\partial A}{\partial \tau} = \varepsilon A + \hat{r} |A|^2 A \quad , \quad (21)$$

with linear coefficient being given by

$$\begin{aligned} \varepsilon &= \frac{\langle \underline{v}_c | \delta \underline{L}(q_c) \underline{u}_c \rangle}{\langle \underline{v}_c | \underline{u}_c \rangle} \\ &= -\frac{(Dq_c^2)^2}{D(D+1)q_c^4} \left[\left(\sqrt{T} + \sqrt{\frac{\alpha^{\text{T}}}{D}} \right) \frac{\delta \alpha}{\sqrt{\alpha^{\text{T}} D}} + f''(j_0^{\text{T}}) \delta j_0 \right] \quad . \end{aligned} \quad (22)$$

For the cubic coefficient we make use of the general formula (cf. e.g. [24])

$$\begin{aligned}
\hat{r} &= \frac{1}{\langle \underline{v}_c | \underline{u}_c \rangle} \langle \underline{v}_c | 4C\{\underline{u}_c, \underline{\Gamma}_a\} + 2C\{\underline{u}_c, \underline{\Gamma}_b\} + 3D\{\underline{u}_c, \underline{u}_c, \underline{u}_c\} \rangle \\
\underline{\Gamma}_a &:= -\frac{1}{\underline{L}(0)} C\{\underline{u}_c, \underline{u}_c\} \\
\underline{\Gamma}_b &= -\frac{1}{\underline{L}(2q_c)} C\{\underline{u}_c, \underline{u}_c\} \quad .
\end{aligned} \tag{23}$$

Taking eqs.(6), (9), and (16) into account we end up with

$$\hat{r} = \frac{(Dq_c^2)^4}{(D-1)q_c^2(Dq_c^2 + \alpha^\top)} \left[\frac{2}{9q_c^2} (f''(j_0^\top))^2 - \frac{1}{2} f'''(j_0^\top) \right] \quad . \tag{24}$$

The sign of this real coefficient determines whether the instability is sub- (positive sign) or supercritical (negative sign). Since the coefficient does not depend on the particular pattern under consideration the conclusion holds for squares and hexagons as well.

Figure 1 reveals that two Turing–Hopf bifurcation points appear at our parameter setting. Eq.(20) tells us that the type of Hopf instability is solely determined by the third derivative of the nonlinear contribution (2). Since for our particular choice (2) the third derivative is negative for large current j_0 , the righthand Turing–Hopf point corresponds typically to a subcritical Hopf bifurcation. Therefore we focus on the lefthand Turing–Hopf point. In order that both codimension one lines yield supercritical behaviour the critical wavenumber q_c has to be large enough in view of eq.(24). Thus, taking eq.(8) into account, the diffusion coefficient D should not exceed a certain threshold value. Altogether, eqs.(20) and (24) result in the constraints

$$f'''(j_0^{\text{TH}}) > 0, \quad \frac{2T}{D-1} > \frac{4(f''(j_0^{\text{TH}}))^2}{9f'''(j_0^{\text{TH}})} \tag{25}$$

on the parameter values for the Turing–Hopf point to be supercritical. These conditions are met for our parameter setting chosen in figure 1. In what follows we concentrate on the lefthand Turing–Hopf point since the weakly nonlinear analysis gives meaningful results only in the vicinity of supercritical bifurcations.

3.2 Turing–Hopf point: square patterns

We are now going to investigate the vicinity of the Turing–Hopf point. Let us first concentrate on patterns with C_4 symmetry, i.e. consider solutions (15) containing a Hopf mode and two Turing modes with orthogonal wave vectors. Then the coupled set of amplitude equations is obtained

$$\begin{aligned}
\frac{\partial B}{\partial \tau} &= \eta B + \hat{\gamma} |B|^2 B + \hat{\sigma} (|A_1|^2 + |A_2|^2) B \\
\frac{\partial A_1}{\partial \tau} &= \varepsilon A_1 + \hat{r} |A_1|^2 A_1 + \hat{d} |A_2|^2 A_1 + \hat{s} |B|^2 A_1, \quad (1 \leftrightarrow 2) \quad ,
\end{aligned} \tag{26}$$

where the notation $(1 \leftrightarrow 2)$ indicates that the equation for the amplitude A_2 is obtained by interchanging subscripts 1 and 2. Linear coefficients ε and η coincide with eqs.(18) and (22), whereas the cubic coefficients $\hat{\gamma}$ and \hat{r} are again given by eqs.(20) and (24). Of course, parameters $(\alpha^\text{H}, j_0^\text{H})$ and (α^\top, j_0^\top) have to be replaced by their values at the Turing–Hopf point $(\alpha^{\text{TH}}, j_0^{\text{TH}})$. There appear in addition three new coupling coefficients for which the general expressions

$$\hat{d} = \frac{1}{\langle \underline{v}_c | \underline{u}_c \rangle} \langle \underline{v}_c | 4C\{\underline{u}_c, \underline{\Gamma}_a\} + 8C\{\underline{u}_c, \underline{\Delta}\} + 6D\{\underline{u}_c, \underline{u}_c, \underline{u}_c\} \rangle$$

$$\begin{aligned}
\hat{s} &= \frac{1}{\langle \underline{v}_c | \underline{u}_c \rangle} \langle \underline{v}_c | 4C\{\underline{u}_c, \tilde{\Gamma}_a\} + 4C\{\tilde{\underline{u}}_c, \tilde{\Delta}^*\} + 4C\{\tilde{\underline{u}}_c^*, \tilde{\Delta}\} + 6D\{\underline{u}_c, \tilde{\underline{u}}_c, \tilde{\underline{u}}_c^*\} \rangle \\
\hat{\sigma} &= \frac{1}{\langle \tilde{\underline{v}}_c | \tilde{\underline{u}}_c \rangle} \langle \tilde{\underline{v}}_c | 8C\{\underline{u}_c, \tilde{\Delta}\} + 4C\{\tilde{\underline{u}}_c, \Gamma_a\} + 6D\{\underline{u}_c, \underline{u}_c, \tilde{\underline{u}}_c\} \rangle
\end{aligned} \tag{27}$$

with

$$\begin{aligned}
\Delta &= -\frac{1}{\underline{L}(\sqrt{2}q_c)} C\{\underline{u}_c, \underline{u}_c\} \\
\tilde{\Delta} &= -\frac{1}{\underline{L}(q_c) - i\omega_c \underline{1}} C\{\underline{u}_c, \tilde{\underline{u}}_c\}
\end{aligned} \tag{28}$$

are valid. Evaluation according to eqs.(6), (9), (12), and (16) yields

$$\begin{aligned}
\hat{d} &= \frac{D^2(\omega_c^{\text{TH}})^2}{D+1} \left[\frac{4}{(q_c^{\text{TH}})^2} (f''(j_0^{\text{TH}}))^2 - f'''(j_0^{\text{TH}}) \right] \\
\hat{s} &= \frac{D(\omega_c^{\text{TH}})^2}{D+1} \left[\frac{2}{(2D+1)(q_c^{\text{TH}})^2} (f''(j_0^{\text{TH}}))^2 - f'''(j_0^{\text{TH}}) \right] \\
\hat{\sigma} &= \frac{D(\omega_c^{\text{TH}})^2}{2} \left[\frac{2}{(2D+1)(q_c^{\text{TH}})^2} \left(1 - i\sqrt{D}(D+2) \right) (f''(j_0^{\text{TH}}))^2 - f'''(j_0^{\text{TH}}) \right] .
\end{aligned} \tag{29}$$

The numerical values of these coefficients determine which type of solution of the amplitude equations turns out to be stable. In order to discuss particular solutions a normalisation in eq.(26) is useful. Since we focus on the supercritical case, $\text{Re}\hat{\gamma} < 0$ and $\hat{r} < 0$, we normalise the principal cubic coefficients to unity by using the rescaling

$$\sqrt{-\hat{r}}A \rightarrow A, \quad \sqrt{-\text{Re}\hat{\gamma}} \exp(-i\text{Im}\hat{\eta}t)B \rightarrow B \quad . \tag{30}$$

Then the imaginary part of the linear coefficient η has been eliminated and

$$1 + ic = \frac{\hat{\gamma}}{\text{Re}\hat{\gamma}}, \quad \sigma = \frac{\hat{\sigma}}{-\hat{r}}, \quad s = \frac{\hat{s}}{-\text{Re}\hat{\gamma}}, \quad d = \frac{\hat{d}}{-\hat{r}} \tag{31}$$

denote the rescaled cubic coefficients. Different types of solutions of the amplitude equations and their stability is now easily examined¹. We just summarise the result of such an analysis.

(i) Hopf mode: The solution develops no spatial dependence

$$A_1 = A_2 \equiv 0, \quad B = \sqrt{\text{Re}\eta} \exp(-ic\text{Re}\eta t) \quad . \tag{32}$$

Existence of such a type of solution requires

$$\text{Re}\eta \geq 0 \quad , \tag{33}$$

whereas stability with respect to perturbations of the A_ℓ modes yields

$$\varepsilon + s\text{Re}\eta < 0 \quad . \tag{34}$$

¹Our stability analysis is restricted to eqs.(26). Such type of stability is sometimes termed internal stability since wavevectors which are not present in the pattern are discarded. The condition is a necessary stability criterion.

(ii) Turing mode (plane wave): The time independent pattern is determined by

$$A_1 = \sqrt{\varepsilon}, \quad A_2 \equiv 0, \quad B \equiv 0 \quad . \quad (35)$$

Its existence calls for

$$\varepsilon \geq 0 \quad . \quad (36)$$

Stability with respect to the Hopf mode B results in

$$\text{Re}\eta + \text{Re}\sigma\varepsilon < 0 \quad (37)$$

whereas stability with respect to A_2 yields a constraint for the nonlinear coupling coefficient

$$d < -1 \quad . \quad (38)$$

(iii) Turing mode (squares): Square patterns are described by the solution

$$A_1 = A_2 = \sqrt{\frac{\varepsilon}{1-d}}, \quad B \equiv 0 \quad . \quad (39)$$

The two complex phases of the amplitudes A_ℓ remain undetermined because of the translation invariance of the system. Stability with respect to the modes A_ℓ yields the constraint

$$|d| < 1 \quad . \quad (40)$$

Then the condition for existence reduces to eq.(36) whereas stability with respect to the B mode results in

$$\text{Re}\eta + 2\varepsilon\text{Re}\sigma < 0 \quad . \quad (41)$$

(iv) Mixed mode (plane waves): The solution of the spatio-temporal periodic pattern reads

$$\begin{aligned} A_1 &= \sqrt{\frac{\varepsilon + s\text{Re}\eta}{1 - s\text{Re}\sigma}} \\ A_2 &\equiv 0 \\ B &= \sqrt{\frac{\text{Re}\eta + \text{Re}\sigma\varepsilon}{1 - s\text{Re}\sigma}} \exp(i\Delta\omega t) \\ \Delta\omega &= -c|B|^2 + \text{Im}\sigma|A_1|^2 \quad . \end{aligned} \quad (42)$$

Stability with respect to mode A_1 and B requires

$$1 - s\text{Re}\sigma > 0 \quad , \quad (43)$$

whereas stability with respect to A_2 yields again eq.(38). Finally the condition for existence of the solution simplifies to

$$\varepsilon + s\text{Re}\eta \geq 0, \quad \text{Re}\eta + \text{Re}\sigma\varepsilon \geq 0 \quad . \quad (44)$$

(v) Mixed mode (squares): The solution reads

$$\begin{aligned} A_1 = A_2 &= \sqrt{\frac{\varepsilon + s\text{Re}\eta}{1 - d - s\text{Re}\sigma}} \\ B &= \sqrt{\frac{\text{Re}\eta(1-d) + 2\text{Re}\sigma\varepsilon}{1 - d - s\text{Re}\sigma}} \exp(i\Delta\omega t) \\ \Delta\omega &= -c|B|^2 + 2\text{Im}\sigma|A_1|^2 \quad . \end{aligned} \quad (45)$$

Stability of the solution yields two constraints involving the nonlinear coefficients only

$$d > -1, \quad 1 - d - 2s\text{Re}\sigma > 0 \quad (46)$$

and one condition on the linear coefficients ε and $\text{Re}\eta$

$$(1 - d + 2\text{Re}\sigma)\varepsilon + (1 + s)(1 - d)\text{Re}\eta > 0 \quad . \quad (47)$$

Then, existence of the solution calls for

$$\varepsilon + s\text{Re}\eta \geq 0, \quad (1 - d)\text{Re}\eta + 2\text{Re}\sigma\varepsilon \geq 0 \quad . \quad (48)$$

Using the explicit expressions (18), (20), (22), (24), and (29) the coefficients (31) are easily evaluated. The list just described presents an overview over the C_4 symmetric patterns in the vicinity of the Turing–Hopf point. The spatially one–dimensional case (cf. e.g. [25]) is covered by items (i), (ii), and (iv) as well, if one discharges the condition on the coefficient d . This latter quantity determines solely the stability of the spatially two–dimensional patterns.

3.3 Turing–Hopf point: hexagonal patterns

Let us consider patterns consisting of three wave vectors having C_3 symmetry. Then, using the ansatz (15) we finally obtain the set of amplitude equations (cf. appendix A)

$$\begin{aligned} \frac{\partial B}{\partial \tau} &= \eta B + \hat{\gamma}|B|^2 B + \hat{\sigma}(|A_1|^2 + |A_2|^2 + |A_3|^2)B \\ \frac{\partial A_3}{\partial \tau} &= \varepsilon A_3 + \hat{b}A_1^*A_2^* + \hat{r}|A_3|^2 A_3 + \hat{g}(|A_1|^2 + |A_2|^2)A_3 + \hat{s}|B|^2 A_3, \end{aligned} \quad (49)$$

$$(1 \rightarrow 2 \rightarrow 3 \rightarrow 1) \quad . \quad (50)$$

The equations for the Turing mode amplitudes are obtained by cyclic permutation ($1 \rightarrow 2 \rightarrow 3 \rightarrow 1$). Because of resonances at second order the amplitude equations contain quadratic contributions too, if a resummation of different orders is performed. The coefficients η , ε , \hat{r} , $\hat{\gamma}$, and $\hat{\sigma}$ coincide with the expressions given in eqs.(18), (22), (20), (24), and (29). For the new coupling coefficients we obtain the general expressions

$$\begin{aligned} \hat{b} &= \frac{2}{\langle \underline{v}_c | \underline{u}_c \rangle} \langle \underline{v}_c | C\{\underline{u}_c, \underline{u}_c\} \rangle \\ \hat{g} &= \frac{1}{\langle \underline{v}_c | \underline{u}_c \rangle} \langle \underline{v}_c | 6D\{\underline{u}_c, \underline{u}_c, \underline{u}_c\} + 4C\{\underline{u}, \underline{\Gamma}_a\} + 4C\{\underline{u}_c, \underline{\Gamma}_c\} + 4C\{\underline{u}_c, \underline{\Omega}\} \rangle \quad , \end{aligned} \quad (51)$$

where the abbreviations²

$$\begin{aligned} \underline{\Gamma}_c &:= -\frac{1}{\underline{\underline{L}}(\sqrt{3}q_c)} C\{\underline{u}_c, \underline{u}_c\} \\ \underline{\Omega} &:= -\left(\frac{1}{\underline{\underline{L}}(q_c)}\right)_{\langle c \rangle} C\{\underline{u}_c, \underline{u}_c\} \end{aligned} \quad (52)$$

² $(1/\underline{\underline{L}}(q_c))_{\langle c \rangle}$ denotes the inverse according to principal decomposition, i.e. the inverse where in the spectral decomposition the singular contribution $\underline{u}_c \otimes \underline{v}_c^*$ is left out.

have been introduced. Using eqs.(6), (9), (12), and (16) the straightforward evaluation yields

$$\begin{aligned}\hat{b} &= -\frac{D(q_c^{\text{TH}})^2}{D+1}f''(j_0^{\text{TH}}) \\ \hat{g} &= \frac{D^2(\omega_c^{\text{TH}})^2}{D+1}\left[\frac{1}{(q_c^{\text{TH}})^2}\left(\frac{3}{4}+\frac{1}{(D+1)^2}\right)(f''(j_0^{\text{TH}}))^2-f'''(j_0^{\text{TH}})\right]\end{aligned}\quad . \quad (53)$$

For the investigation of solutions of eqs.(49) it is again useful to perform the scaling (30), (31) in the supercritical regime. Hence the new coupling coefficients are replaced by

$$b = \frac{\hat{b}}{\sqrt{-\hat{r}}}, \quad g = \frac{\hat{g}}{-\hat{r}} \quad . \quad (54)$$

Discussion of particular solutions is now almost straightforward.

- (i) Hopf mode: Conditions coincide with the previous case, eqs.(32), (33), and (34).
- (ii) Turing mode (plane wave): The pattern and its condition for existence coincides with the previous case (cf. eqs.(35) and (36)). Stability with respect to the modes $A_{2/3}$ and B results in one constraint for the cubic coupling coefficient

$$g < -1 \quad (55)$$

and two conditions on the linear coefficients, namely eq.(37) and

$$\varepsilon(1+g)^2 > b^2 \quad . \quad (56)$$

- (iii) Turing mode (hexagonal patterns): The solution is given by

$$A_\ell = |\bar{\alpha}|\exp(i\varphi_\ell), \quad B \equiv 0 \quad . \quad (57)$$

Because of translation invariance two of the complex phases φ_ℓ of the amplitudes A_ℓ are arbitrary. The pattern is completely specified by the sum of the phases $\phi := \varphi_1 + \varphi_2 + \varphi_3$. For $\phi = 0$ the pattern has C_6 symmetry, i.e. it consists of symmetric hexagons, whereas for $\phi \neq 0$ only C_3 symmetry survives ("triangles").

The fixed point condition for the phase ϕ and its stability yields (cf. appendix B)

$$\begin{aligned}b > 0, \quad \phi = 0, \quad (\text{"hexagons"}) \\ b < 0, \quad \phi = \pi, \quad (\text{"triangles"})\end{aligned} \quad . \quad (58)$$

The remaining existence and stability conditions condense after some algebra (cf. appendix B) in one condition on the cubic coefficients alone

$$1 - 2g > 0 \quad (59)$$

and three conditions involving the linear coefficients

$$\begin{aligned}4(1-2g)\varepsilon &> -b^2 \\ |b| + (1+g)|\bar{\alpha}| &> 0 \\ \text{Re}\eta + 3\text{Re}\sigma|\bar{\alpha}|^2 &< 0 \quad ,\end{aligned} \quad (60)$$

where

$$|\bar{\alpha}| = \frac{|b| + \sqrt{b^2 + 4\varepsilon(1-2g)}}{2(1-2g)} \quad (61)$$

denotes the amplitude of the pattern.

(iv) Mixed mode (plane wave): The solution and its stability with respect to A_1 and B modes reads as in the previous case (cf. eqs.(42) and (43)). Stability with respect to modes $A_{2/3}$ yields one constraint involving the coupling coefficient between the Turing modes

$$g < -1 \quad (62)$$

and a condition on the linear coefficients

$$b^2 < (1+g)^2 \frac{\varepsilon + s\text{Re}\eta}{1 - s\text{Re}\sigma} \quad (63)$$

Finally the condition for the existence of the solution reduces to eq.(44).

(v) Mixed mode (hexagonal patterns): The equations which determine the spatio-temporal pattern read

$$A_\ell = |\bar{\alpha}| \exp(i\varphi_\ell), \quad B = |\bar{\beta}| \exp(i\Delta\omega t) \quad (64)$$

As already mentioned above only the sum of the phases $\phi := \varphi_1 + \varphi_2 + \varphi_3$ characterises the type of the pattern. Evaluation of the condition of existence and stability is not completely straightforward. It is therefore referred to appendix B. One finally finds for the amplitudes of the modes

$$|\bar{\alpha}| = \frac{|b| + \sqrt{b^2 + 4(1-2g-3s\text{Re}\sigma)(\varepsilon + s\text{Re}\eta)}}{2(1-2g-3s\text{Re}\sigma)} \quad (65)$$

and

$$\begin{aligned} |\bar{\beta}|^2 &= \text{Re}\eta + 3\text{Re}\sigma|\bar{\alpha}|^2 \\ \Delta\omega &= 3\text{Im}\sigma|\bar{\alpha}|^2 - c|\bar{\beta}|^2 \end{aligned} \quad (66)$$

The stability and existence constraints lead to one condition involving the nonlinear coupling coefficients only

$$1 - 2g - 3s\text{Re}\sigma > 0 \quad (67)$$

and four conditions which contain in addition the linear coefficients

$$\begin{aligned} 4(1-2g-3s\text{Re}\sigma)(\varepsilon + s\text{Re}\eta) &> -b^2 \\ |b| + (1+g)|\bar{\alpha}| &> 0 \\ \text{Re}\eta + 3\text{Re}\sigma|\bar{\alpha}|^2 &> 0 \\ |b||\bar{\alpha}| - 2(1-2g)|\bar{\alpha}|^2 - 2|\bar{\beta}|^2 &< 0 \end{aligned} \quad (68)$$

The selection rule (58) for the phase applies as well.

4 Results of numerical simulations

We shall now illustrate our findings by simulations of eqs.(1). For the numerical investigation we fix $T = 0.05$ in order to enable a comparison with previous work in one spatial dimension [17]. Usually two Turing–Hopf points appear if the diffusion coefficient D is not too small (cf. figure 1). First of all we have to locate a parameter setting which yields a supercritical Turing–Hopf bifurcation.

In view of eq.(20) the condition for a supercritical Hopf instability, $\text{Re}\hat{\gamma} < 0$, calls for $f'''(j_0) > 0$. Taking the choice (2) into account we arrive at the constraint $j_0 \in [(3 - \sqrt{8})^{1/2}, (3 + \sqrt{8})^{1/2}]$ on the current. Thus the righthand Turing–Hopf point turns out to be subcritical for most values of D . We therefore entirely focus on the lefthand Turing–Hopf point where the Hopf instability can be expected to be supercritical.

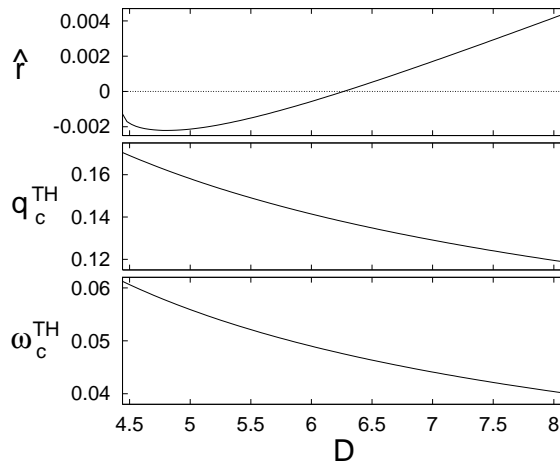


Figure 2: The cubic coefficient \hat{r} at the Turing Hopf point, the critical wavenumber q_c^{TH} and the critical frequency ω_c^{TH} in dependence on the diffusion coefficient D (cf. eqs.(13), (14), and (24)). Turing-Hopf points disappear if $D < (1 + \sqrt{8T})/(1 - \sqrt{8T})$, i.e. at the left hand end of the diagram.

To check for supercriticality of the Turing instability we have to consider the coefficient (24). Figure 2 reveals that supercriticality of the Turing instability is ensured in an intermediate range of diffusion only. Here we fix $D = 5$ which is close to the minimum of the cubic coefficient. Then the location of the supercritical Turing-Hopf point in the parameter plane is according to eqs.(13) given by

$$\alpha^{\text{TH}} = 0.0625 \dots, \quad j_0^{\text{TH}} = 1.4279 \dots \quad . \quad (69)$$

The nonlinear coefficients of the amplitude equations are easily evaluated from eqs.(29) and (53) taking the rescaling (31) and (54) into account. We obtain

$$\begin{aligned} \text{Re}\sigma &= -1.5677 \dots, & \text{Im}\sigma &= -3.9848 \dots, & s &= -2.8676 \dots \\ d &= 6.2974 \dots, & b &= 0.2204 \dots, & g &= -1.2221 \dots \quad . \end{aligned} \quad (70)$$

These numerical values enable us to discuss in detail the outcome of the weakly nonlinear analysis. Since the coupling between orthogonal wave vectors, d , is fairly large, eqs.(38) and (40) tell us that all Turing patterns consisting of plane waves or squares are unstable. Furthermore, the product $s\text{Re}\sigma$ violates the conditions (43), (46), and (67) so that all kinds of mixed modes are unstable as well. Since b is positive eq.(58) implies that hexagons but no triangles appear. Thus we are left with studying the Hopf mode and the Turing mode with hexagonal symmetry. Since the condition (59) involving solely nonlinear coefficients is satisfied, we are left with checking for the conditions on the linear coefficients (eqs.(33), (34), and (60)). Expressing ε and $\text{Re}\eta$ in terms of the deviation from the Turing-Hopf point (cf. eqs.(18) and (22)) the stability conditions result in bifurcation lines which are valid in a neighbourhood of the Turing-Hopf point. Our findings are summarised in figure 3. The constraint (33) caused by the existence of the Hopf mode obviously results in the tangent to the full Hopf bifurcation line (10) (cf. eq.(18)). Thus as a first rough estimate for the validity of the weakly nonlinear analysis we may take the region in parameter space where the tangent approximates well the full bifurcation line, since curvature corrections are neglected in the amplitude equations.

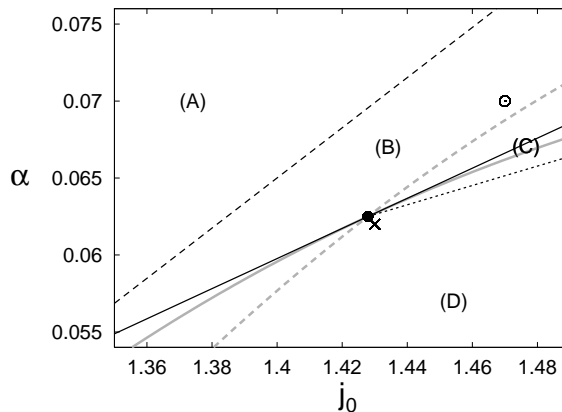


Figure 3: Different stability regimes in the vicinity of the Turing–Hopf point (full circle) in the (j_0, α) parameter plane. Gray: Turing (broken) and Hopf (full) bifurcation line (cf. figure 1). Existence of Hopf mode (full line, cf. eq.(33)), stability of Hopf mode (dotted line, cf. eq.(34)), and saddle–node bifurcation of Turing patterns (broken line, cf. eq.(60₁)). Region (A): trivial solution, region (B): coexistence between trivial solution and Turing pattern, region (C): Turing pattern, region (D): coexistence between Hopf mode and Turing pattern. \times and \circ mark the parameter settings used in figure 4 and 7, respectively.

Concerning the Turing patterns we observe that the stability constraints (60) are satisfied throughout the whole domain bounded by the Turing instability lines, mainly because Res is negative. Hence stable hexagonal patterns exist beyond the Turing instability and no further constraint is imposed. In fact, because of the presence of the quadratic coefficient b the condition (60₁) determines a boundary layer beyond the Turing instability where stable hexagonal patterns also exist. There we expect bistability between the trivial solution and stationary hexagonal patterns. Crossing the boundary determined by eq.(60₁) the Turing pattern is destroyed in a saddle node bifurcation. For the Hopf mode the stability condition (34) confines the region in phase space where stable oscillations appear. However, there exists a wide region beyond the Turing line where hexagonal patterns and homogeneous oscillations coexist.

We compare these results with direct numerical simulations of the full system (1) in the vicinity of the Turing Hopf point. First we concentrate on the region where bistability between hexagonal Turing patterns and Hopf modes are predicted (region (D) in figure 3). Indeed we find stable Turing patterns and Hopf oscillations, depending on the initial condition (cf. figure 4). Close to the Hopf instability lines the Hopf mode has apparently a small basin of attraction and mostly Turing patterns are observed. That is in accordance with the geometry of the bifurcation diagram (figure 3) since the Turing patterns are born in a saddle node bifurcation and have already developed a large basin of attraction if parameter values close to the Hopf line are considered. Nevertheless, deep within the bistability region we observe domain patterns which consist of coexisting patches of hexagonal Turing structures and Hopf oscillations (cf. figure 5 and 6).

Even above the Turing instability line (region (B) in figure 3), where the trivial fixed point is stable we are still able to observe hexagonal Turing patterns (cf. figure 7). Hence bistability between the trivial homogeneous state and Turing patterns prevails in this parameter domain.

Altogether, the features reported so far are in complete agreement with our analytical investiga-

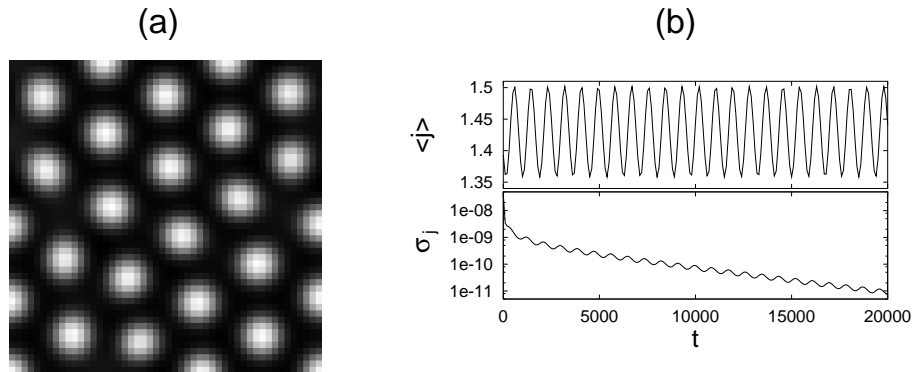


Figure 4: (a) Density plot of stationary Turing pattern for the current density $j(\mathbf{r}, t) = u(\mathbf{r}, t) - a(\mathbf{r}, t)$. (b) Relaxation of a Hopf mode. Time dependence of the spatial average $\langle j \rangle$ of the current and the corresponding variance $\sigma_j = \langle j^2 \rangle - \langle j \rangle^2$. Parameter settings for both parts are the same ($j_0 = 1.43$, $\alpha = 0.062$, $D = 5$, and $T = 0.05$, cf. figure 3), but different initial conditions had been chosen.

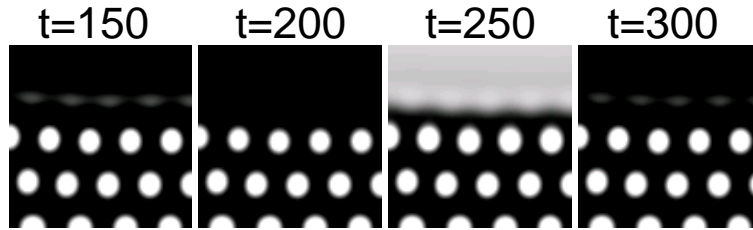


Figure 5: Coexistence pattern between Turing and Hopf state at $j_0 = 1.43$ and $\alpha = 0.045$. The density plots show the current density $j(\mathbf{r}, t)$ at four different times. The time labels refer to figure 6.

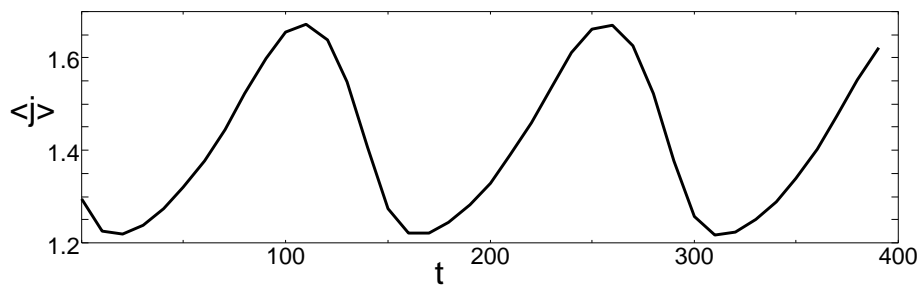


Figure 6: Time dependence of the spatial average of the current density for the state displayed in figure 5.

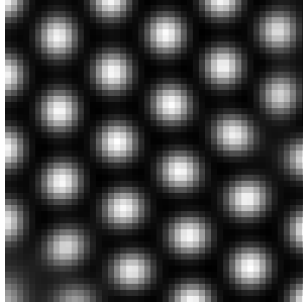


Figure 7: Density plot of the current density $j(\mathbf{r}, t)$ for $j_0 = 1.47$ and $\alpha = 0.07$.

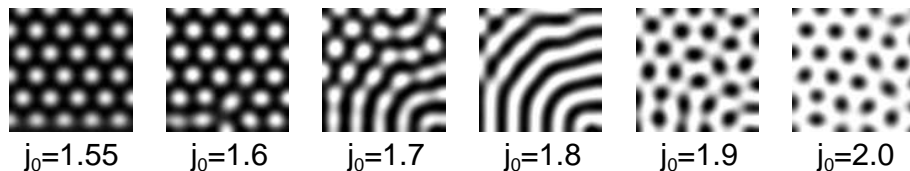


Figure 8: Time independent patterns appearing for different values of the total current j_0 at $\alpha = 0.075$, $T = 0.05$, and $D = 5$: Transition from hot spots (left) to cold spots (right). Simulations have been performed on a system of size 200×200 with Neumann boundary conditions.

tion of the Turing–Hopf instability. However, at larger distance from the Turing–Hopf point scenarios may appear which are not captured by the weakly nonlinear analysis. As a particularly interesting example we mention a transition between two different types of hexagonal patterns, so called cold and hot spots (cf. figure 8). We observe different kinds of time independent stable patterns on changing the total current j_0 . With increasing current the hexagonal structure at low current (hot spots) transforms to a stripe pattern and then changes to a hexagonal pattern where the amplitudes are inverted (cold spots). Upon decreasing the current hysteresis is found. We should mention that this scenario depends on the boundary conditions and the system size and hence might be a genuine feature of the finite system.

5 Conclusions

Combining a linear stability analysis with the weakly nonlinear analysis of Turing–Hopf points we have been able to uncover the structure of the solutions of the reaction–diffusion system (1) on two-dimensional spatial domains. The results have been condensed in a bifurcation diagram which can be confirmed quantitatively by numerical simulations. Because of the size of coupling coefficients between Turing and Hopf modes no mixed modes are observed. In addition, the coupling between the different spatial modes favours hexagonal patterns compared to plane waves and square patterns. There exist large regions of bistability in the neighbourhood of the Turing–Hopf point.

Though only valid locally, our analysis applies to much larger parts of the parameter plane from a qualitative point of view. In fact, domain like coexistence patterns between hexagons and Hopf modes are observed for typical parameter values beyond the linear stability thresholds.

Our findings show that mixed Turing–Hopf modes are unlikely to occur in two spatial dimensions, while pure hexagonal Turing patterns or coexistence modes between Turing patterns and oscillations can easily be found. In terms of the layered semiconductor model this means that spatio–temporal spiking, i.e. the mixed subharmonic Turing–Hopf mode, which has been found in one–dimensional simulations and observed in several semiconductor experiments, is suppressed if the sample has two lateral dimensions of comparable size. It is, however, preferred in samples with one long and one short lateral dimension. Current filamentation in two–dimensional devices thus occurs in form of regular hexagonal stationary Turing patterns rather than spatio–temporal spiking modes. This may be of interest since it allows for the selforganized ordering of small localized current filaments in regular arrays. Also, with increasing current density, the transition between arrays of high–current filaments (hot spots) via stripes to low–current filaments (cold spots) may occur.

Our model describes charge transport in layered semiconductor structures, but is also of more general interest because of its simple generic form. From our approach we can determine the parameter ranges for the various stable spatio–temporal patterns on two–dimensional domains. Since we have derived general expressions for the coupling coefficients, it is not necessary to go through the tedious analytical derivation for each model separately. One can just plug in the details of the particular system in our final expressions (e.g. eq.(19)). Thus the results of our calculation are not limited to the special model (1),(2) but can be easily applied to other nonlinear reaction–diffusion systems.

The actual values of the coupling coefficients determine the type of Turing–Hopf instability, e.g. whether mixed modes, or coexistence solutions appear. We expect that in different parts of the whole parameter space, e.g. upon variation of the diffusion coefficient D or the tunnelling rate T , other types of spatio–temporal patterns may be found. Analysing the corresponding transition points of codimension three along the lines of our paper one may shed more light on the properties of the full model. In this way, instabilities of increasing codimension may finally yield a skeleton of possible bifurcation scenarios, a strategy which has already proven to be successful in understanding low–dimensional dynamical systems (cf. [26] for some example).

Our approach can be generalised to include the effect of sideband instabilities. The corresponding calculations become even more tedious although no principal difficulties arise. Such a complete analysis is required if one aims to check the full stability of the patterns under consideration. For our present model such advanced approaches appear to be dispensable since no sideband instabilities have shown up in numerical investigations.

Acknowledgement

This work was supported by DFG within the framework of "Sonderforschungsbereich 555".

A Derivation of the amplitude equation

For the most cumbersome case, namely the Turing–Hopf instability involving hexagonal patterns, we sketch the derivation of the amplitude equations. The other cases are simpler and follow along similar lines.

Introducing slow time scales $\tau_i = \kappa^i t$ on which the amplitudes A_ℓ and B may depend, the evolution equations (5) and the ansatz (15) yield in first order the eigenvalue problem of the marginally stable modes

$$\underline{\underline{L}}(q_c^{\text{TH}})\underline{\underline{u}}_c = 0, \quad \underline{\underline{L}}(0)\underline{\underline{\tilde{u}}}_c = i\omega_c^{\text{TH}}\underline{\underline{\tilde{u}}}_c \quad . \quad (71)$$

Here $\underline{\underline{L}}(k)$ denotes the matrix (6) evaluated at the Turing–Hopf point. Using the abbreviations (16)

and assuming that the Hopf mode B will not depend on τ_1 , we obtain in second order

$$\begin{aligned}
& \frac{\partial \underline{\Phi}^{(2)}}{\partial t} + \sum_{\ell} \frac{\partial A_{\ell}}{\partial \tau_1} \exp[i\mathbf{q}_{\ell}\mathbf{r}]\underline{\mathbf{u}}_c \\
= & \mathcal{L}\underline{\Phi}^{(2)} + \sum_{\ell\ell'} A_{\ell}A_{\ell'} \exp[i(\mathbf{q}_{\ell} + \mathbf{q}_{\ell'})\mathbf{r}]C\{\underline{\mathbf{u}}_c, \underline{\mathbf{u}}_c\} \\
& + 2 \sum_{\ell} A_{\ell} \exp[i\mathbf{q}_{\ell}\mathbf{r}] (B \exp[i\omega_c^{\text{TH}}t]C\{\underline{\mathbf{u}}_c, \tilde{\underline{\mathbf{u}}}_c\} + c.c.) \\
& + 2|B|^2 C\{\tilde{\underline{\mathbf{u}}}_c, \tilde{\underline{\mathbf{u}}}_c^*\} + (B^2 \exp[2i\omega_c^{\text{TH}}t]C\{\tilde{\underline{\mathbf{u}}}_c, \tilde{\underline{\mathbf{u}}}_c\} + c.c.) \quad .
\end{aligned} \tag{72}$$

\mathcal{L} denotes the linear part of the right hand side in eq.(5). For simplicity the complex conjugate contributions of the ansatz have been taken into account by adopting the convention $A_{-\ell} = A_{\ell}^*$, $\mathbf{q}_{-\ell} = -\mathbf{q}_{\ell}$ with ℓ ranging between -3 and 3 . The secular condition with respect to the Turing modes leads to

$$\langle \underline{\mathbf{v}}_c | \underline{\mathbf{u}}_c \rangle \frac{\partial A_3}{\partial \tau_1} = 2 \langle \underline{\mathbf{v}}_c | C\{\underline{\mathbf{u}}_c, \underline{\mathbf{u}}_c\} \rangle A_1^* A_2^*, \quad (1 \rightarrow 2 \rightarrow 3 \rightarrow 1) \tag{73}$$

since the wavevectors are resonant at second order, $-\mathbf{q}_1 - \mathbf{q}_2 = \mathbf{q}_3$. Here $\underline{\mathbf{v}}_c$ denotes the left-eigenvector according to $\underline{\mathbf{v}}_c^* \underline{\mathbf{L}}(q_c^{\text{TH}}) = 0$. Then, the nonsecular solution of eq.(72) reads

$$\begin{aligned}
\Phi^{(2)} = & \sum_{\ell \neq \ell' > 0} (A_{\ell}A_{\ell'} \exp[i(\mathbf{q}_{\ell} + \mathbf{q}_{\ell'})\mathbf{r}] + c.c.) \underline{\Omega} \\
& + \sum_{\ell \neq \ell' > 0} (A_{\ell}A_{\ell'}^* \exp[i(\mathbf{q}_{\ell} - \mathbf{q}_{\ell'})\mathbf{r}] + c.c.) \underline{\Gamma}_c \\
& + \sum_{\ell > 0} (2|A_{\ell}|^2 \underline{\Gamma}_a + (A_{\ell}^2 \exp[2i\mathbf{q}_{\ell}\mathbf{r}] \underline{\Gamma}_b + c.c.)) \\
& + 2|B|^2 \tilde{\underline{\Gamma}}_a + (B^2 \exp[2i\omega_c^{\text{TH}}t] \tilde{\underline{\Gamma}}_b + c.c.) \\
& + 2 \sum_{\ell} A_{\ell} \exp[i\mathbf{q}_{\ell}\mathbf{r}] (B \exp[i\omega_c^{\text{TH}}t] \tilde{\underline{\Delta}} + c.c.) \quad ,
\end{aligned} \tag{74}$$

where the abbreviations (19), (23), (28), and (52) have been employed.

If we proceed to third order, the equation of motion results in

$$\begin{aligned}
& \frac{\partial \underline{\Phi}^{(3)}}{\partial t} + \sum_{\ell} \frac{\partial A_{\ell}}{\partial \tau_2} \exp[i\mathbf{q}_{\ell}\mathbf{r}]\underline{\mathbf{u}}_c + \left(\frac{\partial B}{\partial \tau_2} \exp[i\omega_c^{\text{TH}}t] \tilde{\underline{\mathbf{u}}}_c + c.c. \right) \\
= & \mathcal{L}\underline{\Phi}^{(3)} + \delta \underline{\mathbf{L}}(q_c^{\text{TH}}) \sum_{\ell} A_{\ell} \exp[i\mathbf{q}_{\ell}\mathbf{r}]\underline{\mathbf{u}}_c + \delta \underline{\mathbf{L}}(0) (B \exp[i\omega_c^{\text{TH}}t] \tilde{\underline{\mathbf{u}}}_c + c.c.) \\
& + 2C \left\{ \sum_{\ell} A_{\ell} \exp[i\mathbf{q}_{\ell}\mathbf{r}]\underline{\mathbf{u}}_c + (B \exp[i\omega_c^{\text{TH}}t] \tilde{\underline{\mathbf{u}}}_c + c.c.) \right\}, \Phi^{(2)} \\
& + D \left\{ \sum_{\ell} A_{\ell} \exp[i\mathbf{q}_{\ell}\mathbf{r}]\underline{\mathbf{u}}_c + (B \exp[i\omega_c^{\text{TH}}t] \tilde{\underline{\mathbf{u}}}_c + c.c.) \right\}, \\
& \sum_{\ell} A_{\ell} \exp[i\mathbf{q}_{\ell}\mathbf{r}]\underline{\mathbf{u}}_c + (B \exp[i\omega_c^{\text{TH}}t] \tilde{\underline{\mathbf{u}}}_c + c.c.) \quad , \\
& \sum_{\ell} A_{\ell} \exp[i\mathbf{q}_{\ell}\mathbf{r}]\underline{\mathbf{u}}_c + (B \exp[i\omega_c^{\text{TH}}t] \tilde{\underline{\mathbf{u}}}_c + c.c.) \quad \} \quad .
\end{aligned} \tag{75}$$

Collecting all contributions containing a single factor $\exp[i\omega_c^{\text{TH}}t]$ we obtain for the secular condition of the Hopf mode

$$\begin{aligned}
& \langle \tilde{\mathbf{v}}_c | \tilde{\mathbf{u}}_c \rangle \frac{\partial B}{\partial \tau_2} \\
= & \langle \tilde{\mathbf{v}}_c | \delta \underline{L}(0) \tilde{\mathbf{u}}_c \rangle B + \langle \tilde{\mathbf{v}}_c | 3D\{\tilde{\mathbf{u}}_c, \tilde{\mathbf{u}}_c, \tilde{\mathbf{u}}_c^*\} + 4C\{\tilde{\mathbf{u}}_c, \tilde{\Gamma}_a\} + 2C\{\tilde{\mathbf{u}}_c^*, \tilde{\Gamma}_b\} \rangle |B|^2 B \\
& + \langle \tilde{\mathbf{v}}_c | 6D\{\underline{\mathbf{u}}_c, \underline{\mathbf{u}}_c, \tilde{\mathbf{u}}_c\} + 4C\{\tilde{\mathbf{u}}_c, \underline{\Gamma}_a\} + 8C\{\underline{\mathbf{u}}_c, \tilde{\Gamma}_c\} \rangle B \sum_{\ell > 0} |A_\ell|^2 \quad . \quad (76)
\end{aligned}$$

In the same way, collecting all contributions containing a plane wave factor $\exp[i\mathbf{q}_\ell \mathbf{r}]$ the secular conditions of the Turing modes turn out to be

$$\begin{aligned}
& \langle \underline{\mathbf{v}}_c | \underline{\mathbf{u}}_c \rangle \frac{\partial A_3}{\partial \tau_2} \\
= & \langle \underline{\mathbf{v}}_c | \delta \underline{L}(q_c^{\text{TH}}) \underline{\mathbf{u}}_c \rangle A + \langle \underline{\mathbf{v}}_c | 3D\{\underline{\mathbf{u}}_c, \underline{\mathbf{u}}_c, \underline{\mathbf{u}}_c\} + 4C\{\underline{\mathbf{u}}_c, \underline{\Gamma}_a\} + 2C\{\underline{\mathbf{u}}_c, \underline{\Gamma}_b\} \rangle |A_3|^2 A_3 \\
& + \langle \underline{\mathbf{v}}_c | 6D\{\underline{\mathbf{u}}_c, \underline{\mathbf{u}}_c, \underline{\mathbf{u}}_c\} + 4C\{\underline{\mathbf{u}}_c, \underline{\Gamma}_a\} + 4C\{\underline{\mathbf{u}}_c, \underline{\Gamma}_c\} + 4C\{\underline{\mathbf{u}}_c, \underline{\Omega}\} \rangle A_3 \sum_{\ell=1,2} |A_\ell|^2 \\
& + \langle \underline{\mathbf{v}}_c | 6D\{\underline{\mathbf{u}}_c, \tilde{\mathbf{u}}_c, \tilde{\mathbf{u}}_c^*\} + 4C\{\underline{\mathbf{u}}_c, \tilde{\Gamma}_a\} + (4C\{\tilde{\mathbf{u}}_c, \tilde{\Delta}^*\} + c.c.) \rangle |B|^2 A_3, \\
& (1 \rightarrow 2 \rightarrow 3 \rightarrow 1) \quad . \quad (77)
\end{aligned}$$

If we re-sum the secular conditions eqs.(73) and (77) of different order we finally obtain the amplitude equations (49) together with the general expressions eqs.(18), (19), (22), (23), (27), and (51) for their coefficients.

B Stability of hexagonal patterns

The analysis of hexagonal patterns is most conveniently performed by rewriting eqs.(49) in terms of moduli $|A_\ell|$ and total complex phase ϕ . After rescaling according to eq.(30) we obtain

$$\begin{aligned}
\frac{\partial B}{\partial \tau} &= \text{Re}\eta B - (1 + ic)|B|^2 B + \sigma(|A_1|^2 + |A_2|^2 + |A_3|^2)B \\
\frac{\partial |A_3|}{\partial \tau} &= \varepsilon |A_3| + b |A_1 A_2| \cos(\phi) - |A_3|^3 \\
& \quad + g(|A_1|^2 + |A_2|^2) |A_3| + s |B|^2 |A_3|, \quad (1 \rightarrow 2 \rightarrow 3 \rightarrow 1) \\
\frac{\partial \phi}{\partial \tau} &= -b |A_1 A_2 A_3| \left(\frac{1}{|A_1|^2} + \frac{1}{|A_2|^2} + \frac{1}{|A_3|^2} \right) \sin(\phi) \quad . \quad (78)
\end{aligned}$$

Inspecting the equation for the phase ϕ we conclude that stationary solutions require $\phi = 0$ or $\phi = \pi$. Linearisation of the phase equation then yields the stability constraint (58). Thus, for stable stationary solutions the condition $b \cos(\phi) = |b|$ is valid.

Inserting the solution (64) into eqs.(78) we get eqs.(66) and

$$0 = \varepsilon + s \text{Re}\eta + |b| |\bar{\alpha}| - (1 - 2g - 3s \text{Re}\sigma) |\bar{\alpha}|^2 \quad . \quad (79)$$

Employing the notation $B = \bar{\beta} \exp(i\Delta\omega t)(1 + \delta B)$ and $|A_\ell| = |\bar{\alpha}|(1 + \delta A_\ell)$, the linear stability of the solution is investigated. The resulting five-dimensional linear system separates into a two-dimensional coupled set of equations

$$\frac{d}{d\tau} \begin{pmatrix} \text{Re}\delta B \\ \sum_\ell \delta |A_\ell| \end{pmatrix} = \begin{pmatrix} -2|\bar{\beta}|^2 & 2\text{Re}\sigma |\bar{\alpha}|^2 \\ 6s|\bar{\beta}|^2 & |b| |\bar{\alpha}| - 2(1 - 2g) |\bar{\alpha}|^2 \end{pmatrix} \begin{pmatrix} \text{Re}\delta B \\ \sum_\ell \delta |A_\ell| \end{pmatrix} \quad (80)$$

and three uncoupled equations for $\text{Im}\delta B$, $\delta A_3 - \delta A_1$, and $\delta A_3 - \delta A_2$. These three equations give rise to a single (degenerate) constraint

$$\varepsilon + s|\bar{\beta}|^2 - |b||\bar{\alpha}| - 3|\bar{\alpha}|^2 < 0 \quad . \quad (81)$$

If we eliminate $|\beta|^2$ using eq.(66) and then employ eq.(79) to eliminate the linear parameters $\varepsilon + s\text{Re}\eta$ condition (81) simplifies to eq.(68₂). The stability conditions for the system (80) require the trace of the matrix to be negative and its determinant to be positive. The condition on the trace coincides with (68₄) whereas the condition on the determinant gives

$$|b| < 2(1 - 2g - 3s\text{Re}\sigma)|\bar{\alpha}| \quad . \quad (82)$$

If we use condition (82) in eq.(79) we obtain the inequality

$$\varepsilon + s\text{Re}\eta > -(1 - 2g - 3s\text{Re}\sigma)|\bar{\alpha}|^2 \quad (83)$$

whereas eq.(79) itself tells us that

$$\varepsilon + s\text{Re}\eta < (1 - 2g - 3s\text{Re}\sigma)|\bar{\alpha}|^2 \quad (84)$$

holds. From both inequalities we conclude that condition (67) is required. Finally we are solving the quadratic equation (79). Existence of a real solution requires eq.(68₁) if the inequality (67) is taken into account. Eq.(65) then denotes one of the solutions of the quadratic equation. The other solution is ruled out by the inequality (82). Now inequality (82) can be dropped since eq.(65) always satisfies this constraint.

References

- [1] M. C. Cross and P. C. Hohenberg, *Rev. Mod. Phys.* **65**, 851 (1993)
- [2] A. S. Mikhailov and A. Y. Loskutov, *Foundations of Synergetics Vol. II*, 2 ed. (Springer, Berlin, 1996)
- [3] H. Kidachi, *Prog. Theor. Phys.* **63**, 1152 (1980)
- [4] P. Kolodner, *Phys. Rev. E* **48**, R665 (1993)
- [5] D. P. Vallette, W. S. Edwards, and J. P. Gollub, *Phys. Rev. E* **49**, R4783 (1994)
- [6] J. J. Perraud, A. De Wit, E. Dulos, P. De Kepper, G. Dewell, and P. Borckmanns, *Phys. Rev. Lett.* **71**, 1272 (1993)
- [7] P. De Kepper, J. J. Perraud, B. Rudovics, and E. Dulos, *Int. J. Bif. Chaos Appl. Sci. Eng.* **4**, 1215 (1994)
- [8] A. Wacker and E. Schöll, *Z. Phys. B* **93**, 431 (1994)
- [9] K. Hess, T. K. Higman, M. A. Emanuel, and J. J. Coleman, *J. Appl. Phys.* **60**, 3775 (1986)
- [10] F. J. Niedernostheide, M. Arps, R. Dohmen, H. Willebrand, and H. G. Purwins, *Phys. Status Solidi B* **172**, 249 (1992)
- [11] F. J. Niedernostheide, H. J. Schulze, S. Bose, A. Wacker, and E. Schöll, *Phys. Rev. E* **54**, 1253 (1996)

- [12] R. Symanczyk, S. Gaelings, and D. Jäger, *Phys. Lett. A* **160**, 397 (1991)
- [13] U. Rau, W. Clauss, A. Kittel, M. Lehr, M. Bayerbach, J. Parisi, J. Peinke, and R. P. Huebener, *Phys. Rev. B* **43**, 2255 (1991)
- [14] J. Spangler, U. Margull, and W. Prettl, *Phys. Rev. B* **45** 12137 (1992)
- [15] E. Schöll, *Nonlinear spatio-temporal dynamics and chaos in semiconductors* (Cambridge University Press, Cambridge, 2001), in print
- [16] A. Wacker, S. Bose, and E. Schöll, *Europhys. Lett.* **31**, 257 (1995)
- [17] M. Meixner, A. De Wit, S. Bose, and E. Schöll, *Phys. Rev. E* **55**, 6690 (1997)
- [18] M. Meixner, S. Bose, and E. Schöll, *Physica D* **109**, 128 (1997)
- [19] M. Meixner, P. Rodin, and E. Schöll, *Phys. Rev. E* **58**, 2796 (1998)
- [20] M. Meixner, P. Rodin, E. Schöll, and A. Wacker, *Eur. Phys. J. B* **13**, 157 (2000)
- [21] A. Alekseev, S. Bose, P. Rodin, and E. Schöll, *Phys. Rev. E* **57**, 2640 (1998)
- [22] S. Bose, P. Rodin, and E. Schöll, *Phys. Rev. E* **62**, 1778 (2000)
- [23] A. Rovinsky and M. Menzinger, *Phys. Rev. A* **46**, 6315 (1992)
- [24] H. Haken, *Synergetics*, (Springer, Berlin, 1983)
- [25] A. De Wit, G. Dewel, and P. Borckmans, *Phys. Rev. E* **48**, R4191 (1993)
- [26] T. Träxler, W. Just, and H. Sauermann, *Z. Phys. B* **99**, 285 (1996)